Pattern Recognition Letters 146 (2021) 108–114

Contents lists available at ScienceDirect

Pattern Recognition Letters

journal homepage: www.elsevier.com/locate/patrec

Three-dimensional choroid neovascularization growth prediction from longitudinal retinal OCT images based on a hybrid model

Qingquan Meng[a,1], Chang Zuo[a,1], Fei Shi[a], Weifang Zhu[a], Dehui Xiang[a], Haoyu Chen[c], Xinjian Chen[a,b,*]

[a] School of Electronics and Information Engineering, Soochow University, Suzhou 215006, China,
[b] State Key Laboratory of Radiation Medicine and Protection, Soochow University, Suzhou 215123, China
[c] Joint Shantou International Eye Center, Shantou University and the Chinese University of Hong Kong, Shantou, China

ARTICLE INFO

Article history:
Received 20 February 2020
Revised 29 July 2020
Accepted 1 March 2021
Available online 12 March 2021

Keywords:
Choroid neovascularization
Growth prediction
Reaction-diffusion model
Hyperelastic biomechanical model
Optical coherence tomography

ABSTRACT

Choroid neovascularization (CNV) is a pathological manifestation of retinal-choroidal diseases such as age-related macular degeneration and pathological myopia, which can cause permanent loss of central vision. Prediction of its growth is important in treatment planning. In this paper, based on longitudinal optical coherence tomography (OCT) volumes, a three-dimensional CNV growth prediction framework is proposed. A hybrid model which combines the reaction-diffusion model and the hyperelastic biomechanical model through mass effect is adopted to characterize the growth of CNV region and its reaction with surround tissues. A treatment factor is also included so that the model can adjust to different treatment plan each patient receives. Tested on a dataset with 6 subjects, each with 12 longitudinal 3D images, the proposed method achieved average true positive rate (TPR), false positive rate (FPR) and Dice coefficient (DC) of 80.0 ± 7.62%, 23.4 ± 8.36% and 78.9 ± 7.54%, respectively, in predicting the future CNV regions, and outperforms those achieved by the single reaction-diffusion model.

1. Introduction

Choroidal neovascularization (CNV) is a pathological manifestation of retinal-choroidal diseases such as wet age-related macular degeneration, pathological myopia, and central serous retinopathy, which can damage central vision and lead to blindness in severe cases. The overexpression of vascular endothelial growth factor (VEGF) in retinal pigment epithelial cells is considered to be crucial with the development of CNV [1,2]. Hence, currently, the most effective treatment for CNV is repeated intravitreal anti-VEGF injections. As this process is long-term and expensive, and complications may be caused by intraviteal injections, treatment planning is important to maximize the efficacy while reduce the cost and risks.

Optical coherence tomography (OCT) [3], as a non-invasive retinal imaging technique which can show the 3D structure of CNV-related pathologies, is ideal for CNV diagnosis and tracking of its progress. Qualitative or quantitative criteria obtained from OCT images have been used in clinical practice for treatment planning, such as to determine the necessity of next injection [4,5]. If accurate prediction of the CNV growth can be achieved based on modeling the change of physiological structure shown in OCT images, the patient's response to the treatment can be analyzed and personalized anti-VEGF treatment plan can be made.

Many existing research on prediction of CNV progress or treatment planning focused on simple indicators such as the retinal thickness, choroidal thickness and volume of intra-retinal of sub-retinal fluids [5,6]. The extensive information contained in the OCT image was ignored by using these simple measurements as an indicator of CNV growth. In [7], based on OCT quantifications of retina and fluids, a machine learning based approach was proposed to predict the retinal response at the end of a standardized 12-week induction phase of anti-VEGF treatment. In [8] and [9], using similar biomarkers, the number of future anti-VEGF injections and prognostic visual acuity were predicted. These methods didn't give the future status of the CNV. Methods for predicting the actual position and range of the future CNV region are very limited. Inspired by the tumor growth modeling methods in [10-12], we first proposed a model-based CNV growth prediction method based on the reaction-diffusion equation and finite-element-method (FEM)

* Corresponding author at: School of Electronics and Information Engineering, Soochow University, Suzhou 215006, China, and State Key Laboratory of Radiation Medicine and Protection, Soochow University, Suzhou 215123, China.
E-mail address: xjchen@suda.edu.cn (X. Chen).
[1] indicates these authors contributed equally

https://doi.org/10.1016/j.patrec.2021.03.006
0167-8655/

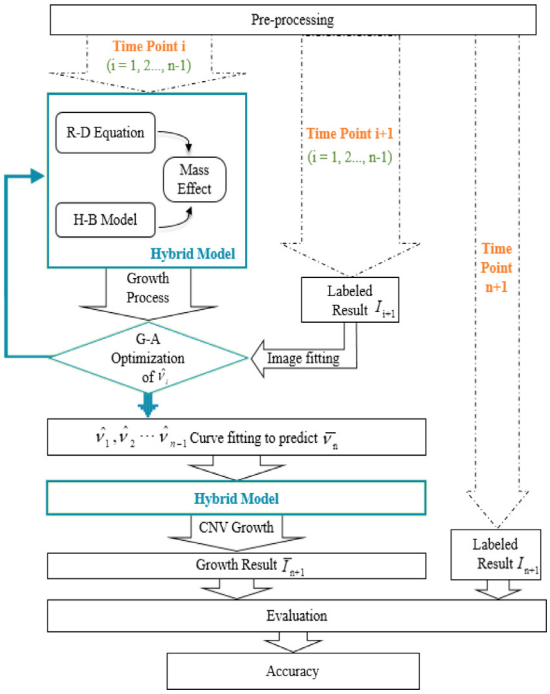

Fig. 1. Flowchart of the proposed method.

[13,14]. However, the performance may be limited by use of the linear mechanical model, which is proper for small deformation but not for large ones.

In this paper, we further improve the CNV growth model by combining the reaction-diffusion model and hyperelastic biomechanical model, so that the interaction between CNV and its surrounding physiological structures are more effectively described. The reaction-diffusion model describes the CNV distribution in space and its temporal development, while the hyperelastic mechanical model is used for simulating stress-strain nonlinear deformations of CNV. Different from the method for tumor growth modeling in [12], which is a simple combination of the two models, the proposed method used the mass effect [15] to effectively integrate them. A personalized treatment factor is also added in the reaction-diffusion equation, allowing drug-induced treatment to contribute to the growth modeling. This paper is an expansion of [16], and more technical details are provided.

2. Method

2.1. Overview

The flow-chart of the proposed method is showed in Fig. 1, including three steps: pre-processing, CNV growth modeling by the hybrid model and prediction. Pre-processing includes registration, segmentation and meshing. In CNV growth modeling, a hybrid model is constructed and the parameters learned from OCT images of the first *n*-1 time points. Optimization is done using the genetic algorithm. At the prediction stage, the model parameter of the last time point is obtained by curve fitting the optimized parameters from the previous multiple time points. Then the predicted CNV region is constructed from the predicted model parameter. The prediction accuracy is evaluated by comparing the prediction with the ground truth label of CNV region of the last time point.

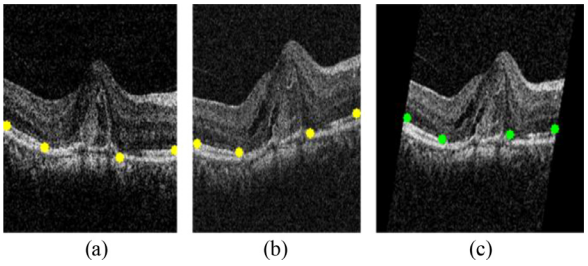

Fig. 2. Registration of longitudinal OCT images. (a) Reference image. (b) Moving image (c) Registration result. Yellow dots indicate manually selected feature points, and green dots indicate feature points after transformation.

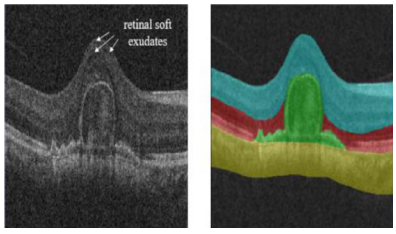

Fig. 3. Image segmentation: (a) Original image. (b) Segmentation result.

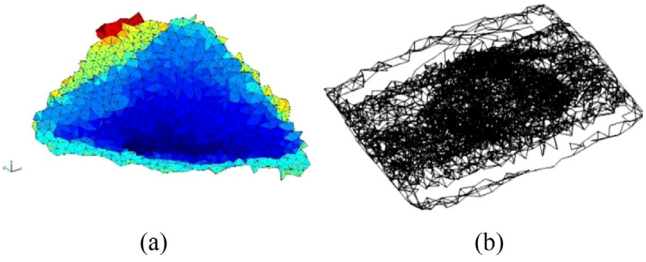

Fig. 4. Meshed OCT image: (a) Tetrahedral decomposition and meshing of CNV region.(c) The gridding frame of retinal area.

2.2. Pre-processing

Registration is first applied to deal with the displacement of the longitudinal data. The OCT image at the 1st time point is used as reference image, and images at all other time points are registered to it. The registration is conducted on 3D OCT images interactively using a rigid transformation [14]. This simple transformation is chosen so that the morphology of CNV is not distorted. Feature points are manually marked on the reference image and the moving image. Bilinear interpolation is adopted to calculate pixel values in the registered images. Fig. 2 shows the registration results.

Segmentation is necessary for locating regions of interest and separating regions with different physiological structures and therefore different growing parameters. In this paper, graph based methods [17,18] with local manual adjustments are used to segment the retina in each 3D image into four parts, as showed in Fig. 3: CNV region (green), outer retinal layer (red), inner retinal layer (cyan) and choroid layer (yellow). Other pathological regions such as soft exudates are ignored and treated as part of the retina tissues.

Next, meshing is conducted so that the model can be solved using FEM. The ISO2Mesh method [19,20] is used to mesh CNV volumes and retinal layers. ISO2Mesh is an open-source mesh generation based on volume and surface, suitable for creating high-quality surfaces and tetrahedral meshes from 3D medical image. Fig. 4 shows the results of meshing.

Table 1
Important notations of the hybrid model.

C	CNV concentration	F	deformation gradient
$\mathbf{D}$	anisotropic diffusion tensor	J	determinant of F
ρ	proliferate rate	I_1	first invariant of the right Cauchy-Green deformation tensor
f_{th}	therapy term	κ	bulk modulus
λ	ratio for efficacy	μ	shear modulus
r_{FS}	final stability ratio	σ	Cauchy stress tensor
ε	Green-Lagrange strain tensor	f	gradient force

2.3. The hybrid model

The proposed model for CNV growth is a combination of the reaction-diffusion model and the hyperelastic biomechanical model. The former focuses on the distribution of CNV in space over time, while the latter treats CNV as a hyper-viscoelastic material that interacts with surrounding tissues. The two models are linked through mass effect. COMSOL Multiphysics® Software (COMSOL Inc.) is used to solve the partial differential equations by FEM [21,22]. The multifrontal massively parallel solver (MUMPS) is used. Important notations in this section are summarized in Table 1.

A. the reaction-diffusion equation

Define $c$as the CNV concentration, and the reaction-diffusion equation depicts its change over time [23]:

$$\frac{\partial c}{\partial t} = \nabla \cdot (\mathbf{D}\nabla c) + \rho c(1-c) - \beta f_{\text{th}} \tag{1}$$

where $\mathbf{D}$ represents the anisotropic diffusion tensor with three components D_x,D_y and D_z.ρ is the proliferate rate, which can take different value at each time point. The first and second term stand for CNV invasion and the logistic proliferation [24]. The third term f_{th} is the therapy term. $\beta = 1$ only when anti-VEGF treatment is applied at the current time point, and otherwise $\beta = 0$.

$$f_{\text{th}} = \left(\frac{\alpha}{1+e^{\lambda t}} + r_{FS}\right) \cdot c \tag{2}$$

where α is a constant for individualizing model, λ stands for the ratio for efficacy, and r_{FS} represents the final stability ratio, and $r_{FS} \in [0, 1]$. At the beginning of treatment (with small t), the f_{th} curve can be approximately linear [25], while at the post-treatment stage, the curve tends to be flat. When $t = 0$, $\alpha/2 + r_{FS}$ is the initial concentration ratio, and this value is learned from the data as $|V_t - V_{t+1}|/|V_t|$, where V_t and V_{t+1}represents the size of CNV volumes before and after anti-VEGF injection. Substituting (2) into (1) gives (3):

$$\frac{\partial c}{\partial t} = \nabla \cdot (\mathbf{D}\nabla c) + \rho c(1-c) - \left(\frac{\alpha}{1+e^{\lambda t}} + r_{FS}\right) \cdot c \tag{3}$$

Without loss of generality, the initial value of c can be set arbitrarily as long as this value is also used as the threshold to obtain the binary prediction of CNV volume. In our experiments, it is set as 4.0×10^3.

B. the hyperelastic biomechanical model

This model can be used for simulating stress-strain in large and nonlinear deformations [26]. It adapts well to the characteristics of biological tissues and can greatly help to simulate the growth of biological tissues, cells or disease areas.

We assume that after the static equivalent transformation, only the stress nearby the exerted location is significantly affected. Therefore, we use modified Saint-Venant-Kirchhoff constitutive law to model the slightly incompressible and isotropic material of CNV. The strain energy density function and the constitutive equation are given as

$$\varepsilon = \frac{1}{2}(F^T F - I) \tag{4}$$

$$\psi(\varepsilon) = \frac{1}{2}\kappa(J-1)^2 + \frac{1}{2}\mu Tr(I_1 - 3) \tag{5}$$

where $\varepsilon$is the Green-Lagrange strain tensor, and F is the deformation gradient with $J = \det(F)$. F can be decomposed multiplicatively to a isochoric deformation component$\bar{F}$by $F = (J^{1/3}I)\bar{F} = J^{1/3}\bar{F}$ and $J^{1/3}I$is the volumetric deformation tensor [27]. The first and the second terms in (5) account for the volumetric and isochoric elastic response, respectively. I_1 is the first invariant of the right Cauchy-Green deformation tensor. Tr represents the trace, κandμ are the bulk modulus and shear modulus respectively. The second Piola-Kirchhoff (PKII) stress tensor ($S = \partial\psi/\partial\varepsilon$) can provide the nonlinear stress-strain relation [26]. To characterize the different compositions, in our CNV growth model, the four retinal regions are assigned different mechanical parameters. The empirical values as follows:$\kappa_{\text{CNV}} = 7kPa$, $\kappa_{\text{choroid}} = 6kPa$, $\kappa_{\text{outer\_layer}} = 6kPa$, $\kappa_{\text{inner\_layer}} = 0.7kPa$, $\mu_{\text{CNV}} = \mu_{\text{choroid}} = 5 \times 10^3 N/m^2$, and $\mu_{\text{outer\_layer}} = \mu_{\text{inner\_layer}} = 1 \times 10^3 N/m^2$.

C. mass effect

The invasion process of CNV leads to a gradual change in blood vessel density between regions. In biology, this inhomogeneous distribution of substance move across the membrane leads to gradient difference. Then, diffusion occurs when the neovascularization performs a net movement from high concentration to low. Equilibrium is reached when there is no longer any net movement in the area. Since the growth of CNV is a slowly changing process, whose rate is relatively small in a short period of time, its deformation can be regarded as an internal equilibrium system. According to Newton's first law, in an internal equilibrium system, there is a set of equilibrant (no net-forces) exerted on the object. The general formula of the static equilibrium equation is as follows:

$$\sum \vec{\mathrm{F}} = 0 \tag{6}$$

Furthermore, CNV growing is not merely the diffusion process that solutes spread along a concentration gradient. It is often accompanied by changes in the total mass and volume of substances. Therefore, as deformation rate of CNV growth is slow enough to remain in internal equilibrium, the static equilibrium equation is used to simulate mass and volume changes during the process. This relates the gradient force f, generated by the normalized anisotropic concentration c in reaction-diffusion equation and the Cauchy stress tensor σ in hyperelastic biomechanical model [23]:

$$div(\sigma) + f = 0;\ f = -\xi\nabla c;\ \sigma = J^{-1}FSF^T \tag{7}$$

where$\xi$is a constant that depends on the biological property.

Table 2
Results of CNV prediction in TPR(%), FPR(%), DC(%) and RVD(%).

	Patient-Label			Mean±Std			
T-group	*1*	*2*	*3*	*Hybrid Model*	*R-D Model[14]*	*DNN Model*	*Cubic Fitting*
TPR	86.0	64.1	83.0	**77.7 ± 9.7**	73.2 ± 3.1	65.3 ± 4.9	N/A
FPR	12.0	39.0	26.4	**25.8 ± 11.1**	27.5 ± 4.6	48.5 ± 7.8	N/A
DC	86.1	62.8	80.8	**76.5 ± 9.9**	73.0 ± 3.6	60.1 ± 8.1	N/A
RVD	2.3	4.2	5.6	**3.3 ± 2.3**	18.4 ± 14.7	23.2 ± 20.3	17.8 ± 15.2
R-group	*4*	*5*	*6*	*Hybrid Model*	*R-D Model[14]*	*DNN Model*	*Cubic Fitting*
TPR	79.7	87.1	80.2	**82.4 ± 3.4**	77.6 ± 2.6	73.6 ± 4.0	N/A
FPR	18.2	24.9	20.5	**21.1 ± 2.7**	24.2 ± 2.1	45.8 ± 22.1	N/A
DC	80.6	83.6	80.0	**81.4 ± 1.6**	76.8 ± 2.4	71.1 ± 8.9	N/A
RVD	2.2	8.7	0.5	**3.8 ± 3.5**	9.7 ± 10.5	17.6 ± 19.0	40.7 ± 38.7

2.4. Parameter optimization

For longitudinal OCT images from each subject, we construct a personalized hybrid model from the first N-1 time points. Specifically, we find the optimal values of parameter set $\theta = \{D_x, D_y, D_z, \rho_1, \rho_2 \cdots \rho_{N-2}\}$ from the ground truth of CNV regions. The following objective function, combining the true-positive volume fraction (TPVF) and false-positive volume fraction (FPVF) over all time points i is minimized:

$$Obj(\theta) = \sum_{i=1}^{N-2} [w_1 \cdot (1 - TPVF_i) + w_2 \cdot FPVF_i]$$

$$TPVF = \frac{|ov_{i+1,\theta}|}{|I_{i+1,\theta}|}, FPVF = \frac{|\bar{I}_{i+1,\theta}| - |ov_{i+1,\theta}|}{|I_{i+1}|},$$

$$ov_{i+1,\theta} = \bar{I}_{i+1,\theta} \cap I_{i+1} \quad (8)$$

where I_{i+1}represents the set of voxels labeled as CNV in ground truth, and $\bar{I}_{i+1,\theta}$ represents the set of CNV voxels predicted based on parameter set θ. w_1 and w_2 represent the weights for 1-TPVF and FPVF, respectively, and $w_1 + w_2 = 1$. Higher w_1 results in higher TPVF and higher FPVF, and vice versa. The weights are set equally as 0.5 in this paper to achieve balanced true positive and false positive rates in prediction results.

The genetic algorithm [28,29] is adopted for optimization. The population size, iteration times/generations and tolerance were set as 20, 200 and 1×10^{-100} respectively. The CNV concentration computed by COSMOL is iteratively output to MATLAB® (The Mathworks Inc.) for optimization through LiveLink.

2.5. Prediction

In parameter prediction part, allometric regression [30] and B-spline fitting is used to estimate the proliferate rate ρ_{N-1} for the last time period from the optimal proliferate rates $\rho_1, \rho_2 \cdots \rho_{N-2}$. The results of both curve fitting methods are averaged to get the final estimate. Based on ρ_{N-1}, the prediction image of the last time point $\bar{I}_N$ is calculated using the hybrid model. Finally, the prediction accuracy is evaluated by comparing $\bar{I}_N$ with the ground truth label I_N.

3. Experimental results

OCT images of AMD patients with CNV were collected by ZEISS 4000 OCT scanner monthly over a year, resulting in longitudinal data with 12 OCT volumes ($N = 12$). The actual size of the sampling area for 3D-image was $6 \times 6 \times 2\text{mm}^3$, with $512 \times 128 \times 1024$ voxels (width×Bscans×height) of $11.72 \times 46.88 \times 1.95\ \mu\text{m}^3$ voxel size. In the study, subjects were randomly put into two groups: treatment group (T-group) and reference group (R-group) as in Fig. 5. They had different treatment plans of repeated anti-VEGF injection. This study was approved by the ethical review committee of Joint Shantou International Eye Center and conducted in accordance with the tenets of the Helsinki Declaration. Written informed consent was obtained from each subject.

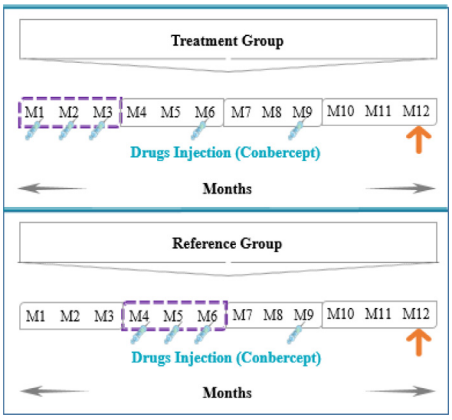

Fig. 5. Two different therapy groups during the same interval: M1 to M12 mean Month1 to Month12. Monthly treatment is illustrated in purple. In months not marked, placebo was injected. The orange arrow means the last month, which is the time of assessment.

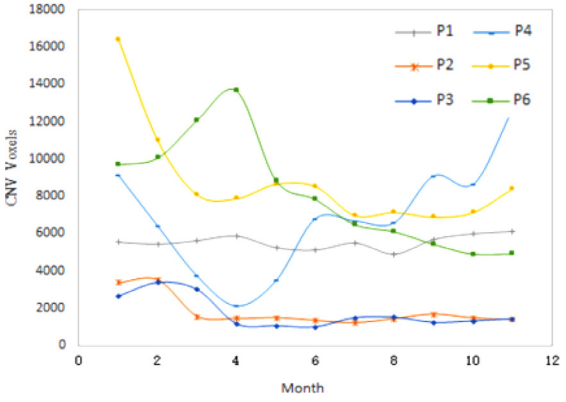

Fig. 6. Curves showing CNV voxels change of different patients.

Our test dataset includes three subjects (P1-P3) from the T-group and three (P4-P6) from the R-group. The curves showing the change of CNV size are plotted in Fig. 6. The curves are very different, probably affected by many factors such as the stage of the pathology and the response to anti-VEGF injections. This shows that it is crucial to have a flexible model that is individualized to each single subject.

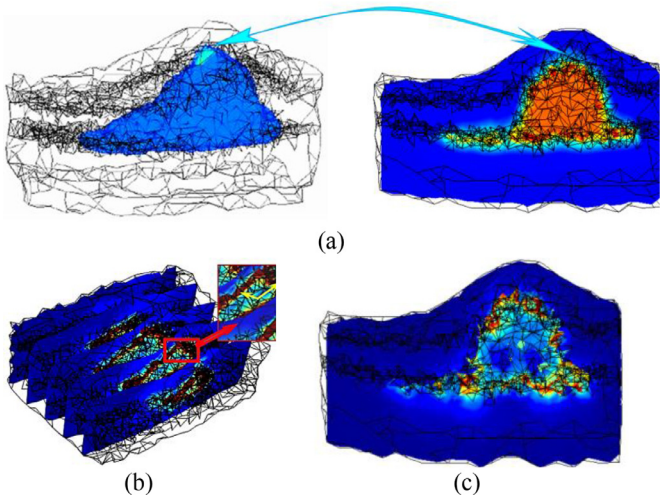

Fig. 7. CNV growth modeling results: (a) Isosurfaces of CNV concentration (left) and the concentration sectional view of all segmented blocks (right). (b) sectional plane of CNV stress distribution. Yellow arrows show the increase of stress toward the boundary of CNV region. (c) The Mises stress distribution pattern. Warmer color represents higher values.

An example of the concentration image is illustrated in Fig. 7(a), where warmer color in the center represents area with higher density, and the concentration decrease towards surrounding areas, colored by orange to blue. The double-headed arrow across the image indicates that corresponding positions share the same concentration. Stress distribution is shown in Fig. 7(b) and (c). It can be found that near the boundary of CNV region the stress is much larger than inside the CNV region, while almost no forces are transmitted to the outside.

The 3D CNV growth results depicted in 3D and 2D are showed in Fig. 8, where each row corresponds to one subject. It be seen that the overlapping of the prediction and ground truth (blue) accounts for a large proportion of the total volume, indicates high accuracy. The proposed method can well predict the location, shape, size of the CNV.

Table 2 shows the performance indices in terms of TPR, FPR, Dice coefficient (DC), and relative volume difference (RVD), calculated as follows:

$$\begin{aligned} \mathrm{TPR} &= \frac{|\bar{I}_{12} \cap I_{12}|}{|\bar{I}_{12}|}, \ \mathrm{FPR} = \frac{|\bar{I}_{12} - \bar{I}_{12} \cap I_{12}|}{|R| - |I_{12}|} \\ \mathrm{DC} &= \frac{2|\bar{I}_{12} \cap I_{12}|}{|\bar{I}_{12}| + |I_{12}|}, \ \mathrm{RVD} = \frac{||\bar{I}_{12}| - |I_{12}||}{|I_{12}|} \end{aligned} \tag{9}$$

where $\bar{I}_{12}$and $I_{12}$are the set of CNV voxels in predicted results and the ground truth for the 12th time point, respectively, and R is the set of voxels inside the retina. $|\cdot|$represents the number of pixels in the set.

Results of the proposed method are compared with those achieved by reaction-diffusion (R-D) model [14], a deep neural network (DNN) model, and a curve fitting model. The DNN model extracts features from 3D OCT data of previous time points, and combine them to predict the future CNV. More details can be found in Appendix. The curve fitting model serves as a baseline. A cubic function is fitted to the total CNV volume of the first 11 time points and the CNV volume at 12th time point is obtained by extrapolation. With this baseline, only the size of CNV is predicted, and therefore only RVD can be calculated.

For both T-group and R-group, the proposed hybrid model outperforms all other methods in accuracy. The total average TPR, FPR, DC, and RVD over the six subjects are 80.0 ± 7.62%, 23.4 ± 8.36%, 78.9 ± 7.54% and 3.58 ± 2.68%, respectively.

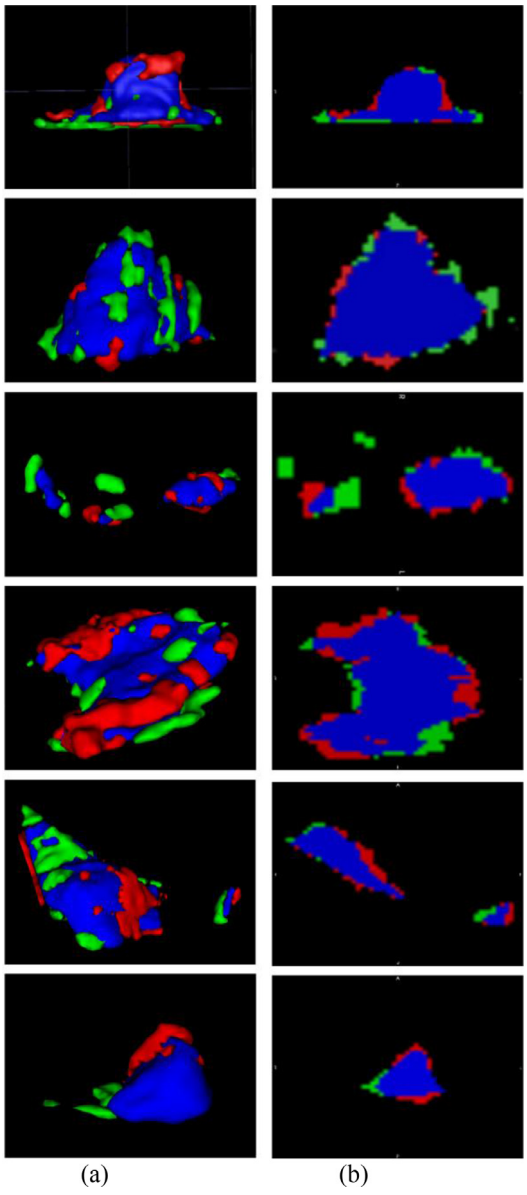

Fig. 8. Comparison of prediction result (red) and ground truth label (green) of CNV region, where blue represents the overlapping. (a) 3D rendering. (b) 2D projection. (For interpretation of the references to colour in this figure legend, the reader is referred to the web version of this article.)

The analysis of the trained model accuracy over time is shown in Fig. 9, representing how well the model fitted to the training data. Each point in the chart represents the respective index (DC, TPVF or FPVF) obtained by the optimized model for one patient at a particular time point. It is found that although most points are within the range of mean±sd, the values of P2 deviate a lot from the average, as showed by blue diamond shapes. This corresponds to the worst performance indices of P2 showed in Table 2. By further inspection at the OCT images, we find that the low performance may be caused by the following reasons. First, the quality of image acquisition is the poorest among all data. There are big differences between adjacent slices, probably caused by unstable fixation. This leads to weak correlation both spatially and temporally, which makes registration difficult and eventually hampers the model fitting. In addition, the CNV region of this subject is relatively small-sized (Fig. 6) during whole treatment period, which

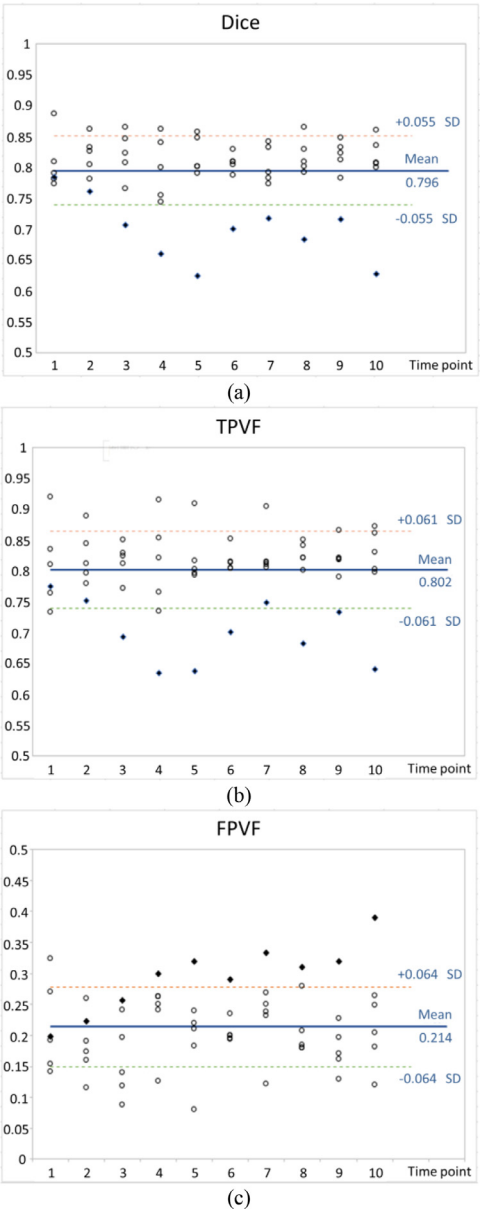

Fig. 9. Model fitting accuracy over time (a) Dice coefficient. (b) TPVF. (c) FPVF. Each point in the chart represents the respective index obtained by the optimized model for one patient at a particular time point. The blue diamonds represent data for Patient 2, which has the worst performance. (For interpretation of the references to colour in this figure legend, the reader is referred to the web version of this article.)

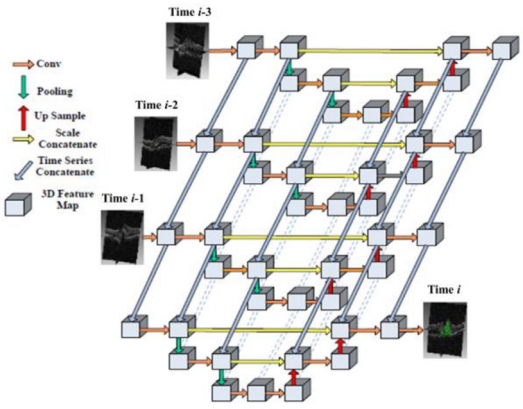

Fig. 10. Time series 3D U-Net.

makes the false positive relatively big. Nevertheless, the RVD for P2 is still low, indicating that the total CNV volume is predicted quite precisely.

4. Conclusions

In this paper, we have proposed a novel 3D CNV growth prediction approach with a hybrid model, based on longitudinal volumetric OCT scans. In CNV growth modeling stage, the mass effect in slow deformation is used to combine a bio-mechanical model of hyper viscoelastic material with reaction diffusion equation. The reaction-diffusion equation provides proliferation and spread information of the pathological region, while biomechanical model includes the information of different structures and functions of the hyper-viscoelastic materials inside the retina. This makes the proposed hybrid model fit better to the longitudinal data than a single reaction-diffusion model. In addition, in the reaction-diffusion equation, a personalized treatment factor is added, making the model applicable to patients with different treatment plans.

Compared with the deep learning method, the proposed method achieves much better results based on the small training dataset, while less intensive training is needed. What's more, the proposed method, based on physical models, is highly explainable and can be further explored to investigate the physiopathology of CNV.

There are some limitations in this work. First, currently the performance of the proposed method has some dependency on the image quality. In the future, to make the method more robust, we'll invest on better pre-processing methods, especially automatic registration and segmentation methods. Secondly, the size of dataset is small. We'll test and improve the method in a bigger dataset in future works. As the CNV progress is also affected by some random factors, with more data, we'll consider integrating methods such as probabilistic modelling [31] in the current framework.

Experiments on clinical data reached promising prediction performance. It is expected that the predicted CNV size, location and shape can help ophthalmologists in prognosis, and making personalized treatment plans. In the future, we'll also investigate prediction with data from less and earlier time points, so that the clinicians can find non-responders to anti-VEGF treatments at an early stage, switch to other treatments and avoid the costs and possible complications caused by repeated injections.

Declaration of Competing Interest

None.

Acknowledgments

This work was supported in part by the National Key R&D Program of China under Grant 2018YFA0701700, and in part by the National Natural Science Foundation of China (NSFC) under Grant 61622114, 61971298, 61771326.

Appendix: The DNN model for comparison

Fig. 10 shows the structure of time series 3D U-Net used for comparison in Section 3. This network uses 3D U-Nets to extract features from each time point, and the features are concatenated over time. Then CNV prediction is output at the last 3D U-Net structure.

The first 11 OCT volumes and the CNV ground truth from all 6 patients are used to train the network, and CNV prediction for the 12th time point is the test output. Due to limitations of GPU memory, each time in training, only 3 OCT volumes consecutive in time are fed in the DNN to predict the CNV in the next time point.

The network was trained for 500 epochs, with Adam optimizer with initial value learning rate of 0.0001.

References

[1] K. Spilsbury, K.L. Garrett, W.Y. Shen, I.J. Constable, P.E. Rakoczy, Overexpression of vascular endothelial growth factor (vegf) in the retinal pigment epithelium leads to the development of choroidal neovascularization, Am. J. Pathol. 157 (1) (2000) 135–144.

[2] N. Kwak, N. Okamoto, J.M. Wood, P.A. Campochiaro, VEGF is major stimulator in model of choroidal neovascularization, Invest. Ophthalmol. Vis. Sci. 41 (10) (2000) 58–64.

[3] D. Huang, E.A. Swanson, C.P. Lin, J.S. Schuman, C.A. Puliafito, Opt. coherence tomogr. 254 (5035) (1991) 1178–1181 Science.

[4] P.J. Rosenfeld, A.E. Fung, G.A. Lalwani, et al., Visual acuity outcomes following a variable-dosing regimen for ranibizumab (LucentisTM) in neovascular AMD: the PrONTO study, Invest. Ophthalmol. Vis. Sci. 47 (13) (2006).

[5] H. Oubraham, S.Y. Cohen, S. Samimi, et al., Inject and extend dosing versus dosing as needed: a comparative retrospective study of ranibizumab in exudative age-related macular degeneration, Retina 31 (2011) 26–30.

[6] S.J. Ahn, S.J. Woo, K.E. Kim, K.H. Park, Association between choroidal morphology and anti-vascular endothelial growth factor treatment outcome in myopic choroidal neovascularization, Invest. Ophthalmol. Vis. Sci. 54 (3) (2013) 2115–2122.

[7] H. Bogunovic, M.D. Abramoff, L. Zhang, M. Sonka, Prediction of treatment response from retinal OCT in patients with exudative age-related macular degeneration, in: Proceedings of the Ophthalmic Medical Image Analysis International Workshop 2014, 2014, pp. 129–136.

[8] H. Bogunovic, S.M. Waldstein, T. Schlegl, et al., Prediction of anti-VEGF treatment requirements in neovascular AMD using a machine learning approach, Invest. Ophthalmol. Vis. Sci. (58) (2017) 3240–3248.

[9] U. Schmidt-Erfurth, H. Bogunovic, A. Sadeghipour, et al., Machine learning to analyze the prognostic value of current imaging biomarkers in neovascular age-related macular degeneration, Ophthalmology Retina 2 (2018) 24–30.

[10] O. Clatz, M. Sermesant, P.-Y. Bondiau, H. Delingette, S.K. Warfield, G. Malandain, N. Ayache, Realistic simulation of the 3D growth of brain tumors in MR images coupling diffusion with biomechanical deformation, IEEE. Trans. Med. Imaging 24 (10) (2005) 1334–1346.

[11] X. Chen, R.M. Summers, J. Yao, FEM Based 3D tumor growth prediction for kidney tumor, IEEE. Transac. Biomed. Eng. 58 (3) (2011) 463–467.

[12] X. Chen, R.M. Summers, J. Yao, Kidney tumor growth prediction by coupling reaction-diffusion and biomechanical model, IEEE. Transac. Biomed. Eng. 60 (1) (2013) 169–173.

[13] S. Zhu, X. Chen, F. Shi, D. Xiang, W. Zhu, H. Chen, 3D choroid neovascularization growth prediction based on reaction-diffusion model, SPIE Med. Imag. 9788 (2016) 978807.

[14] S. Zhu, F. Shi, D. Xiang, W. Zhu, X. Chen, H. Chen, Choroid neovascularization growth prediction with treatment based on reaction-diffusion model in 3D OCT images, IEEE. J. Biomed. Health Inform. 21 (6) (2017) 2168–2194.

[15] A. Mohamed, C. Davatzikos, Finite element modeling of brain tumor mass–effect from 3D medical images, in: G. Gerig (Ed.), Medical Image Computing and Computer-Assisted Intervention - MICCAI 2005, LNCS, vol. 3749, Springer, Berlin, Heidelberg, 2005.

[16] C. Zuo, F. Shi, W. Zhu, H. Chen, X. Chen, in: 3D Choroid Neovascularization Growth Prediction With Combined Hyperelastic Biomechanical Model and Reaction-Diffusion model. Fetal, Infant and Ophthalmic Medical Image Analysis, Springer, Cham, 2017, pp. 142–149.

[17] F. Shi, X. Chen, H. Zhao, W. Zhu, D. Xiang, E. Gao, M. Sonka, H. Chen, Automated 3-D retinal layer segmentation of macular optical coherence tomography images with serous pigment epithelial detachments, IEEE Trans. Med. Imaging 34 (2) (2015) 441–452.

[18] X. Chen, M. Niemeijer, L. Zhang, K. Lee, M.D. Abramoff, M. Sonka, Three-dimensional segmentation of fluid-associated abnormalities in retinal OCT: probability constrained graph-search-graph-cut, IEEE Trans. Med. Imag. 31 (8) (2012) 1521–1531.

[19] Fang, Q., ISO2Mesh: A 3D surface and Volumetric Mesh Generator For MATLAB/octave, http://iso2mesh.sourceforge.net/cgi-bin/index.cgi.

[20] M. Wang, X. Liu, X. Wu, Visual classification by l1-hypergraph modeling, IEEE Trans Knowl Data Eng 27 (9) (2015) 2564–2574.

[21] K.J. Bathe, Finite Element Procedures, Prentice Hall, 1996.

[22] C. Luo, Z. Li, K. Huang, J. Feng, M. Wang, Zero-shot learning via attribute regression and class prototype rectification, IEEE. Trans. Image Process. 27 (2) (2018) 637–648.

[23] C. Hoge, C. Davatzikos, G. Biros, An image-driven parameter estimation problem for a reaction-diffusion glioma growth model with mass effects, J. Math Biol. 56 (6) (2008) 793–825.

[24] J. Friedman, T. Hastie, R. Tibshirani, Additive logistic regression: a statistical view of boosting, Ann. Stat. 28 (2) (1998) 337–407.

[25] D.F. Martin, M. Klein, J. Haller, Preclinical and phase 1A clinical evaluation of an anti-VEGF Pegylated Aptamer (EYE001) for the treatment of exudative age-related macular degeneration, Retina, J. Retin. Vitr. 22 (2002) 143–152.

[26] G.A. Holzapfel, Nonlinear solid mechanics: a continuum approach for engineering science, Kluwer Acad. Pub. 37 (4) (2002) 489–490.

[27] K.C.L. Wong, R.M. Summers, E. Kebebew, J. Yao, Tumor growth prediction with hyperelastic biomechanical model, physiological data fusion, and nonlinear optimization, Med. Image Comput. Comput. Assist Interv. (MICCAI 2014) 17 (2014) 25–32 Springer, Switzerland.

[28] K. Deb, A. Pratap, S. Agarwal, T. Meyarivan, A fast and elitist multiobjective genetic algorithm: NSGA-II, IEEE Trans. Evolu. Comput. 6 (2) (2002) 182–197.

[29] C. Luo, B. Ni, S. Yan, M. Wang, Image classification by selective regularized subspace learning, IEEE Trans Multimedia 18 (1) (2016) 40–50.

[30] R. Keskinen, Exponential growth and allometric equations, J. Theor. Biol. 98 (4) (1982) 675–677.

[31] M. Wang, Y. Gao, K. Lu, Y. Rui, View-based discriminative probabilistic modeling for 3D object retrieval and recognition, IEEE Trans. Image Process. 22 (4) (2013) 1395–1407.